ELSEVIER

Journal of Power Sources 88 (2000) 206–218

JOURNAL OF POWER SOURCES

www.elsevier.com/locate/jpowsour

Lithium polymer electrolyte pyrite rechargeable battery: comparative characterization of natural pyrite from different sources as cathode material

E. Strauss [a], G. Ardel [a], V. Livshits [a], L. Burstein [b], D. Golodnitsky [a,b,*], E. Peled [a,b]

[a] *School of Chemistry, Tel Aviv University, Ramat-Aviv, Tel Aviv, 69978, Israel*
[b] *Wolfson Applied Materials Research Center, Tel Aviv University, Tel Aviv, 69978, Israel*

Received 9 July 1999; received in revised form 26 November 1999; accepted 6 December 1999

Abstract

The thermal and electrochemical behavior of pyrite as an electrode material for rechargeable lithium polymer electrolyte batteries has been investigated. The samples of pyrite from several different sources were characterized by thermogravimetric analysis (TGA), SEM, X-ray photoelectron (XPS) and electrochemical methods. As determined by thermogravimetric measurements, the pyrite samples of ''vendors A and G'' were highly stable up to 500°C. The weight loss of FeS_2 at 500°C did not exceed 1.3%. The decomposition of the ''vendor E'' sample, including eight phase transitions, starts at about 100°C and is caused by the surface impurities of pyrite, such as iron oxides, hydroxides and sulfates. These influence the OCV and the first discharge of the Li/CPE/FeS_2 cell. It is noteworthy that the performance characteristics, such as Li/Fe ratio, faradaic efficiency and charge–discharge overpotential of the Li/composite polymer electrolyte (CPE)/10-μm-thick cathode pyrite cells were found to be almost independent of the degree of contamination and, consequently, of the pyrite source during 30 cycles.

Keywords: Lithium polymer electrolyte; Pyrite; Battery

1. Introduction

There is an increasing demand for the development of high-energy density batteries for portable electronic devices as well as for electric vehicles and energy storage. Lithium batteries are attractive in this regard as they offer higher energy density compared to other rechargeable systems. In rechargeable lithium and lithium-ion batteries, the cathodes that are on the market are made of expensive synthetic compounds capable of reversibly intercalating the lithium ions. Natural pyrite warrants interest as a cathode material in lithium batteries because of its nearly unlimited abundance, low cost and high theoretical energy density when coupled to lithium. We have recently demonstrated that an all-solid-state lithium battery containing composite polymer electrolyte (CPE) and a pyrite-based cathode is a promising candidate for EV and energy-storage applications. The theoretical energy density of this battery is nearly twice that of lithium/lithiated Co, Mn, V and Ni oxide batteries. The projected specific energy for practical value of a large Li/CPE/FeS_2 battery is 250 W h/kg [1,2].

One of the major obstacles to the commercialization of lithium polymer electrolyte and lithium-ion batteries for EV application is the high cost of these batteries. The material cost of the Li/CPE/FeS_2 battery is about $40/kW h (excluding the case), a sixth that of lithium-ion batteries and other lithium polymer electrolyte batteries (estimated at $250/kW h). There are two reasons for such a low cost (similar to that of the lead-acid battery): the use of LiI as a salt at $20/kg while others use $LiPF_6$ or lithium imide at about $250/kg and the use of a natural ore (pyrite) as a cathode material at $0.5/kg while others use lithiated metal oxides at $30/kg to $80/kg [5].

The mineral pyrite, FeS_2, is present in the most ancient magnetic rocks and in more recent sedimentary deposits. There are different sources of natural pyrite: Logrono

* Corresponding author. School of Chemistry, Tel Aviv University, Ramat-Aviv, Tel Aviv, 69978, Israel. Tel.: +972-3-640-8438; fax: +972-3-640-9293.
E-mail address: golod@ccsg.tau.ac.il (D. Golodnitsky).

0378-7753/00/$ - see front matter
PII: S0378-7753(99)00526-1

mines in Spain, USA (Missouri; Shasta County, CA); Canada (Ontario), Russia (Urals), etc. [3]. One of the possible paths of pyrite oxidation in the presence of water [3] is described by Eq. 1:

$$2FeS_2 + 7O_2 + 2H_2O \rightarrow 2FeSO_4 + 2H_2SO_4. \quad (1)$$

Formation of thiosulfate and sulfite intermediates, and sulfur as a side product of pyrite oxidation have been reported [3].

The use of pyrite as cathode material in batteries presumes a detailed knowledge of the phase diagram and the thermal stability of the mineral. For the purpose of developing a high-energy density rechargeable lithium battery, special attention must be paid to the homogeneity range and impurities. The quality of pyrite, which varies dramatically among sources and even between lots from the same source, may cause persistent problems for the manufactures of Li/FeS_2 batteries. It was found that a high-voltage spike, which may result in the instability of the cell, accompanies the first discharge of the Li/composite polymer or gel electrolyte/pyrite battery. In addition, it is well known that the reproducibility of the cathode behavior is improved with the use of pyrite of highly uniform physical and chemical properties.

The main aim of this work is to characterize natural pyrite from different sources and suppliers as possible

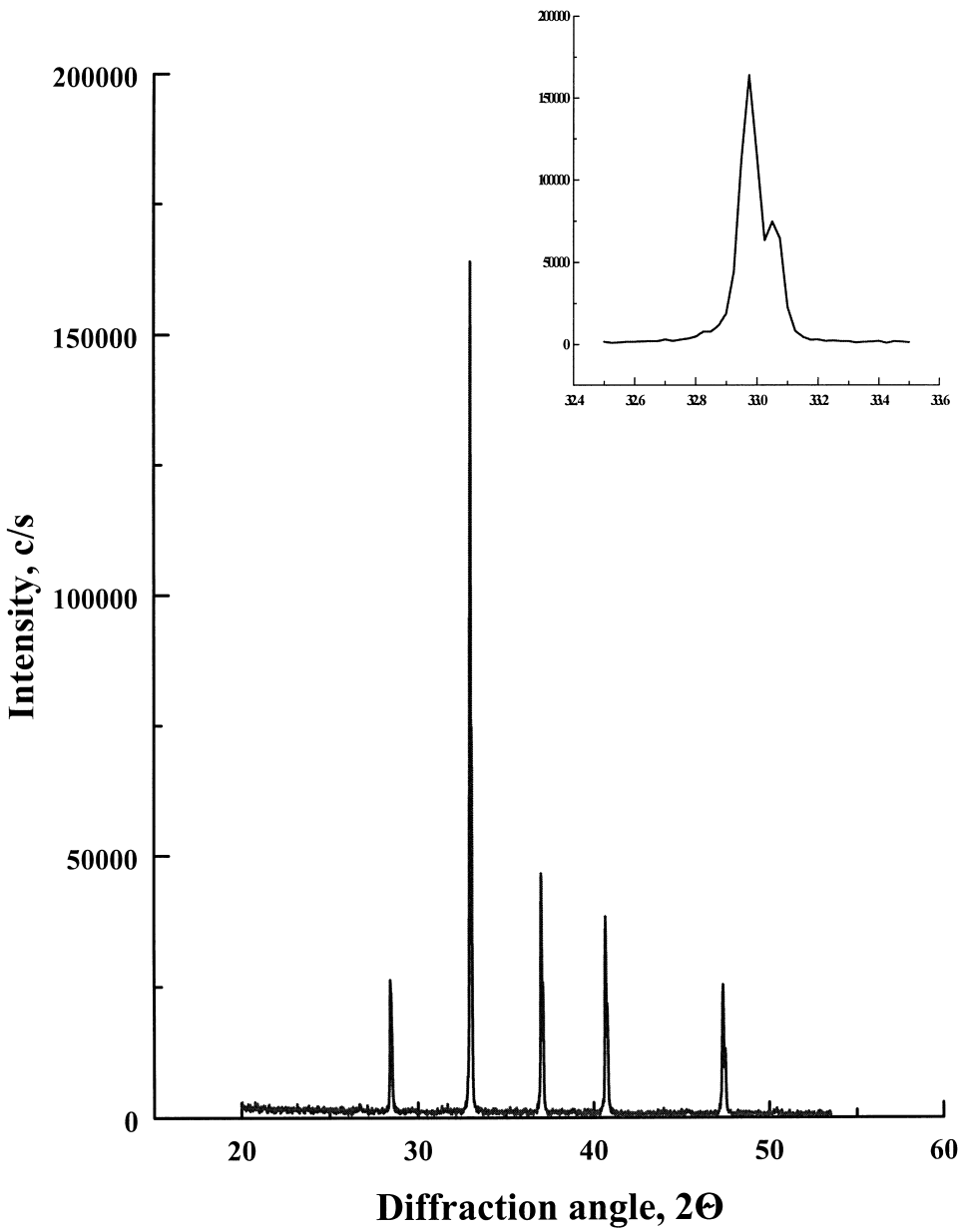

Fig. 1. XRD pattern of natural pyrite (vendor G).

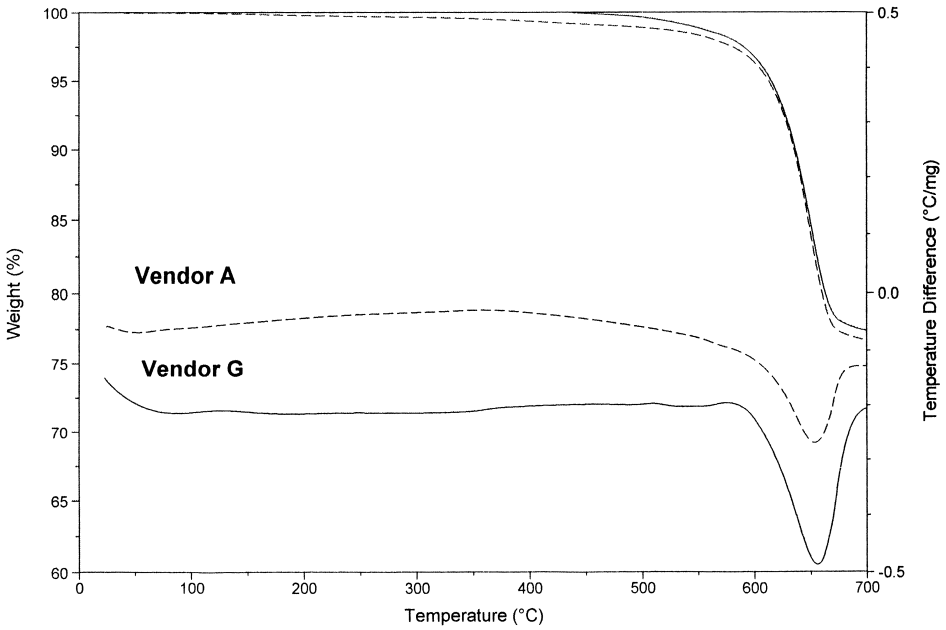

Fig. 2. TGA/DTA thermograms of natural pyrite.

cathode material for all-solid-state lithium batteries. The X-ray photoelectron (XPS), thermogravimetric analysis (TGA)/differential thermal analysis (DTA), SEM, X-ray diffraction (XRD) and electrochemical methods are used. BET measurements were made with the use of a NOVA 2200 surface analyzer (Quantachrom).

2. Experimental

The electrochemical cells studied comprise a lithium anode, CPE consisting of (LiI)$P(EO)_{20}$EC 9% v/v Al_2O_3 (where v/v is a volume concentration) and a composite FeS_2 cathode, which contains 50% v/v of CPE and 50% v/v natural pyrite from various sources and vendors, which were chosen arbitrary and marked A, B, C, E, F and G. The samples of vendors A, B, F and G were chemically pretreated according to different procedures, which were not specified by the suppliers. The electrolytes were prepared from poly(ethylene oxide) [P(EO); Aldrich, average molecular weight 5×10^6], which was vacuum-dried at 45°C to 50°C for about 6 h. The LiI (Aldrich) was vacuum-dried at 200°C to 230°C for about 8 h. All subsequent handling of the materials took place under an argon

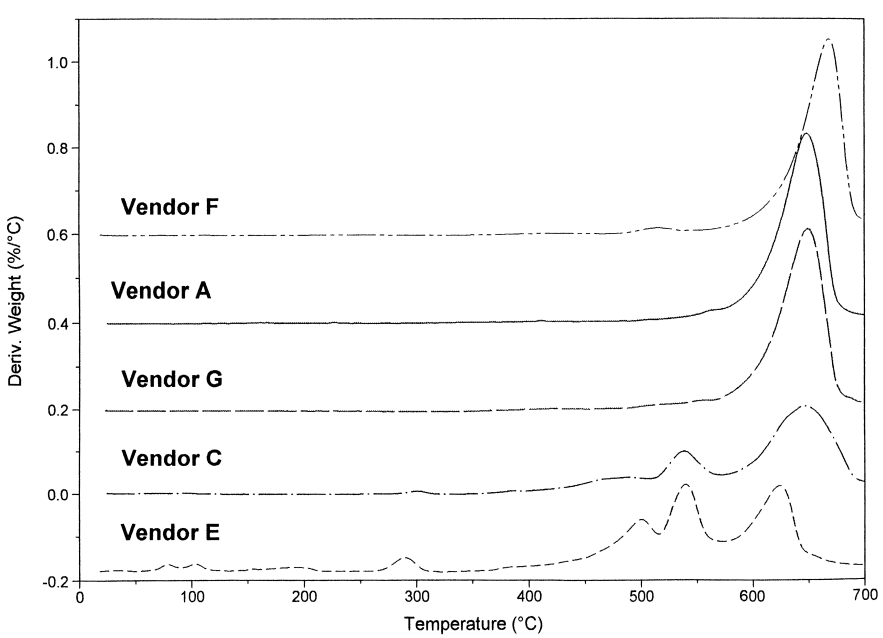

Fig. 3. DTG thermograms of natural pyrite from different sources.

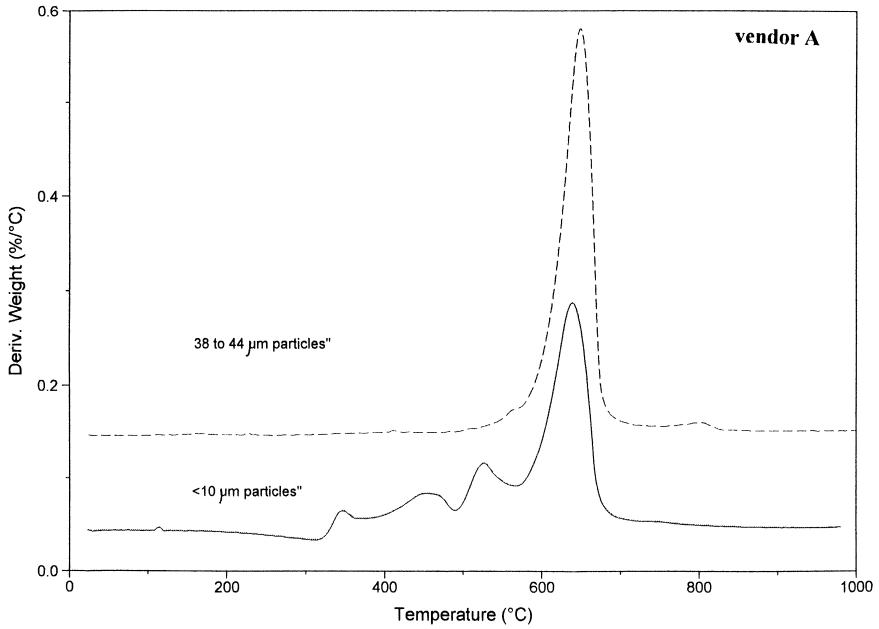

Fig. 4. DTG thermograms of different particle size natural pyrite (vendor A).

atmosphere in a VAC glove box with water content < 10 ppm. The particle size of pristine pyrites is less than 44 μm. BET measurements showed that the surface area of this pyrite is 0.3 m^2/g. The surface area of finely ground less than 10 μm pyrite particles used for thin-cathode lithium batteries is 2.3 m^2/g.

In order to obtain uniform particle size, dry and wet methods were used. For large particles (38–44 μm), the pristine pyrite was sieved and the desired fraction isolated. For particles smaller than 38 μm, which cause problems on dry sieving, the wet method is used. Acetonitrile or cyclopentanone is added to the powder and the mixture is stirred and decanted. For more effective separation of the undesired smallest particles, 0.03–0.1 g/l of Triton X was added to the slurry. The polymer electrolyte and the cathode were prepared as described elsewhere [4]. The final thickness of the solvent-free CPE films was 100 μm. The cathode foil was prepared from pristine, 38–44 μm or < 10 μm ball-milled pyrite powder. All investigations were performed in the 0.95 cm^2 cell, which permitted the

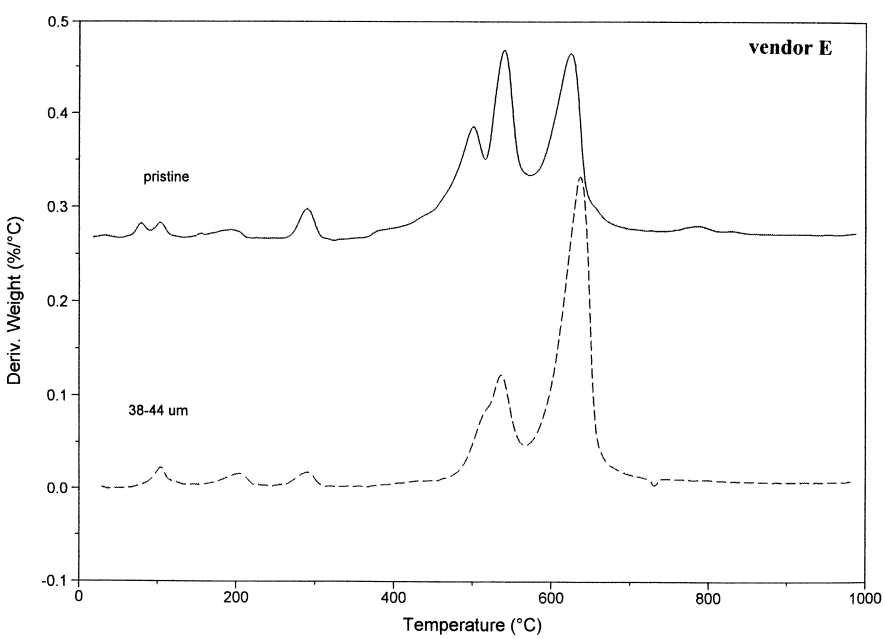

Fig. 5. DTG thermograms of pristine natural pyrite and after separation of small particles (vendor E).

Table 1
TGA data of pyrites from different sources up to 1000°C

Pyrite source	Particle size (μm)	Total weight loss up to 1000°C (%)	1st weight loss (°C/%)[a]	2nd weight loss (°C/%)[a]	3rd weight loss (°C/%)[a]	4th weight loss (°C/%)[a]	5th weight loss (°C/%)[a]	6th weight loss (°C/%)[a]	7th weight loss (°C/%)[a]
E	< 44	29.7	80 (0.36)	100 (0.41)	178 (0.5)	290 (0.85)	498 (6.3)	540 (7)	624.3 (10.6)
E	38–44	27.7		105 (0.64)	206.4 (0.7)	291.8 (0.62)		536.9 (6.4)	636.9 (16)
C	< 44	25.9			301.5 (0.2)	385.8 (0.31)	489.5 (2.8)	538.4 (4.3)	646.7 (15.8)
C	< 10	26					354.8 (0.4)	532 (2.6)	648.2 (19.2)
A	38–44	25.9						562 (shoulder)	648.3 (23.9)
A	< 10	25.8				346 (0.6)	453 (3.4)	527 (4.1)	638.4 (15.4)
G	< 70	25						550 (1.2)	649.8 (21.3)
F	< 70	24.7					429.6 (0.2)	517.3 (0.64)	668.4 (21.9)

[a]The first number shows the temperature of weight loss. The number in parentheses indicates weight loss percent.

sandwiching of the CPE film between a lithium (Foote Mineral) anode and a composite cathode (the detailed procedure of cathode preparation may be found in Ref. [5]). The cells were held under spring pressure inside the hermetically sealed glass vessel. Before each experiment, cells were equilibrated at a given temperature for at least 2 h. The batteries were cycled at 135°C with the use of a Maccor series 2000 battery test system.

Samples for simultaneous TGA–DTA were transferred from the glove box in a sealed vessel just before each measurement. The sample compartment was flushed with dried, UHP argon at all times. The TGA tests were carried out with a TA Instruments module SDT 2960. TGA–DTA runs were recorded at a scan rate of 20°/min up to 700°C. XRD data were obtained with the use of a Phillips PW 1710 diffractometer with Cu Kα radiation. Films were mounted on a single-crystal quartz slide and sealed from the atmosphere with 7-μm-thick aluminum film. A JEOL SEM was used for surface topology study. The X-ray photoelectron (XPS) measurements of the pyrite samples were performed with a monochromatic Al Kα source (1486.6 eV) in UHV (2.5×10^{-10} Torr pressure) with the use of a 5600 Multi-Technique System (Physical Electronics, USA).

3. Results and discussion

Large and quite beautiful crystals of pyrite occur in nature, for instance, in the Urals. Fig. 1 shows a pyrite powder diffractogram measured with Cu Kα radiation.

Table 2
Temperature of decomposition of iron-sulfur and iron-oxygen compounds R.C. Weast (Ed.), Handbook of Chemistry and Physics, CRC Press.

Name	Formulae	Temperature decomposition (°C)
Iron (II) hydroxide	$Fe(OH)_2$	150–200
Iron (III) hydroxide	$Fe(OH)_3 \rightarrow Fe_2O_3$	500
Iron (III) hydroxide oxide	$FeO(OH) - 5H_2O$	136
Iron (II, III) oxide	Fe_3O_4	1538
Iron (III) oxide	Fe_2O_3	1565
Iron (III) oxide, hydrate	$Fe_2O_3 \cdot xH_2O - xH_2O$	350–400
Iron (II) sulfate, pentahydrate	$FeSO_4 \cdot 5H_2O - 5H_2O$	300
Iron (II) sulfate, heptahydrate	$FeSO_4 \cdot 7H_2O - 3H_2O$	56.8
	$FeSO_4 \cdot 7H_2O - 6H_2O$	90
	$FeSO_4 \cdot 7H_2O - 7H_2O$	300
Iron (III) sulfate	$Fe_2(SO_4)_3$	480
Iron (III) sulfate, enneahydrate	$Fe_2(SO_4)_3 \cdot 9H_2O - 7H_2O$	175
Iron (II) sulfate	$FeSO_3 \cdot 3H_2O$	250
Iron (III) hydrosulfate	$Fe_2O_3 \cdot 4SO_3 \cdot 9H_2O - 6H_2O$	80

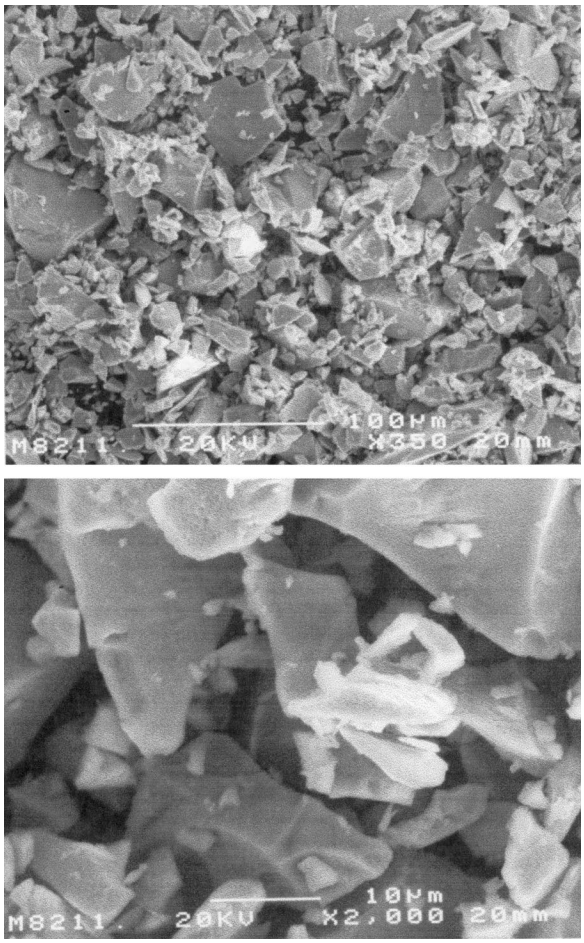

Fig. 6. SEM micrograph of the pristine pyrite (vendor G).

Well-defined doublets specific to pyrite are observed, indicating ordered structure of the material.

It should be pointed out that pyrite is one of the few sulfide minerals, having a molar volume smaller than that of iron sulfates ($V_{FeSO4}/V_{FeS2} = 80/24$) [3]. Thus, a film formed by iron sulfate provides protection of pyrite from oxidation. On the other hand, the presence of surface compounds may cause persistent problems for the manufacture of Li/FeS_2 batteries.

It has been found [6] that the compositional homogeneity range in the natural $Fe–S_2$ system is limited by the stoichiometric composition and typically is 0.5 mol% shifted to the Fe-rich side. Pyrite (grain size of the order < 10 μm) starts to decompose at 300°C. The decomposition process occurs in several steps at 390°C, 440°C, 500°C and 520°C [6]. This complex mechanism was explained by reactions involving single sulfur atoms and sulfur dumbbells on the surface whose bonding energies are different from that of sulfur in the bulk [6].

Simultaneous differential thermal analysis of the five types of pyrite from different sources was performed. Some of the experimental data are presented in Figs. 2–5 and Table 1. As can be seen from Fig. 2, DTA and TG curves of vendors A and G are essentially identical. Ther-

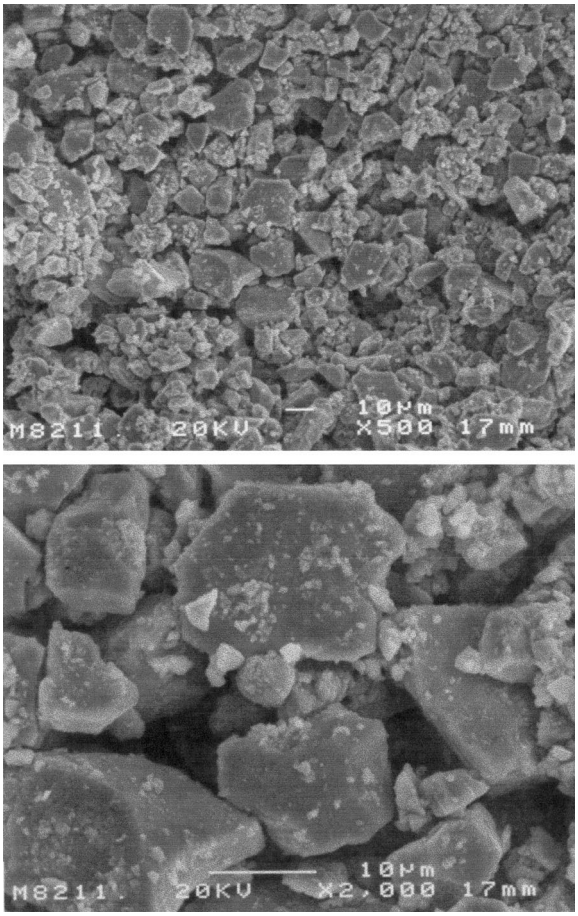

Fig. 7. SEM micrograph of the finely ground pyrite (vendor C) after separation of small particles (wet procedure).

mograms show that the main weight loss (about 23%), appearing as a sharp peak on the derivative thermogravimetry (DTG) curve, occurs at above 640°C (Fig. 3). It is accompanied by a strong endotherm (Fig. 2) and is attributed [10] to the decomposition of pyrite to $FeS_{1.14}$ according to reaction (2)

$$FeS_{2} > FeS_{1.14} + 0.43\,S_2 \quad (2)$$

The measured weight loss (23.9%) is in good agreement with the theoretical value (22.98%) for the decomposition of pyrite to $FeS_{1.14}$. Similar behavior was found for pyrite of vendor F. The decomposition of vendor C pyrite (Fig. 3) starts at about 530°C and a scarcely visible peak appears on DTG run at 300°C. The DTG thermogram of the vendor E sample (Fig. 3) is much more complicated. A very small shoulder at above 530–540°C, preceding the decomposition of pyrite samples of vendors A and G is exhibited by clear peaks on the DTG curves of vendor C and especially vendor E samples. The decomposition process of the latter sample starts at about 100°C and the main peak of pyrite destruction splits into three roughly equal weight-loss comparable DTG peaks (Fig. 3). Ultimately seven phase transitions accompanied by a weight loss of initial material are clearly observed on the DTG/DTA curve of a pristine vendor-E sample up to 700°C. (Fig. 5, Table 1). Almost all the transitions are endothermic. These weight changes can be attributed to surface contamination as can be seen from the Table 2 and from the XPS analysis [5, 7]. The first low-temperature transition (80–90°C) is attributable to the loss of six molecules of water by iron (II) sulfate heptahydrate or iron (III) hydrosulfate (Table 2) [8]. The subsequent weight losses at about 105°C, 178°C and 200°C are associated with partial water loss by iron hydroxide oxide and iron (III) sulfate enneahydrate and the possible decomposition of iron (II) hydroxide. The DTG peak at 292°C is close to the temperature of complete dehydration of iron (II) sulfate, pentahydrate. A small weight loss of 0.4% at 350°C may be due to dehydration of iron (III) oxide hydrate and the weight loss observed at 490°C is associated with the decomposition of iron (III) sulfate. The DTG traces of all pyrite samples under investigation show clear peaks over the range of 517°C to 540°C preceding the main peak of pyrite decomposition. We believe that this thermal transition is related to the surface decomposition of FeS_2 as was shown in [6].

It is highly unusual to find a naturally occurring substance used directly as a principal ingredient in a chemical system requiring components with extremely uniform particles. In order to obtain more uniform distribution of pyrite particles, wet and dry methods of particle separation

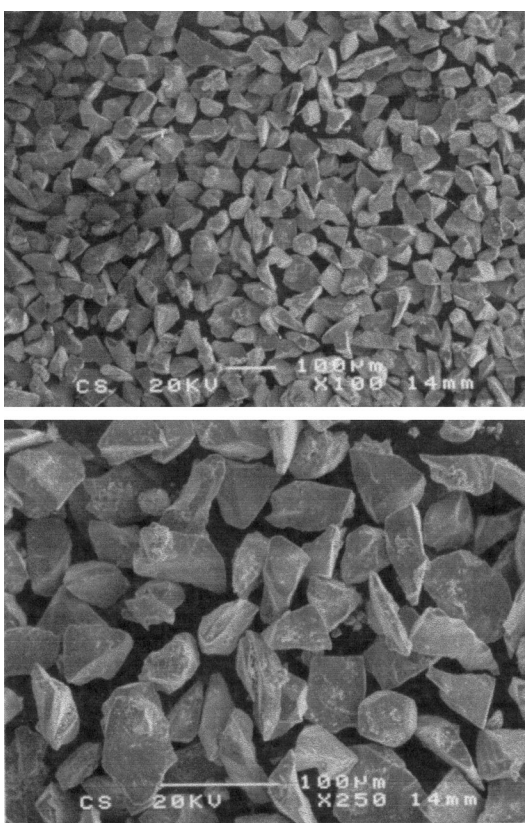

Fig. 8. SEM micrograph of the < 44 μm pyrite (vendor C) after separation of small particles (dry procedure).

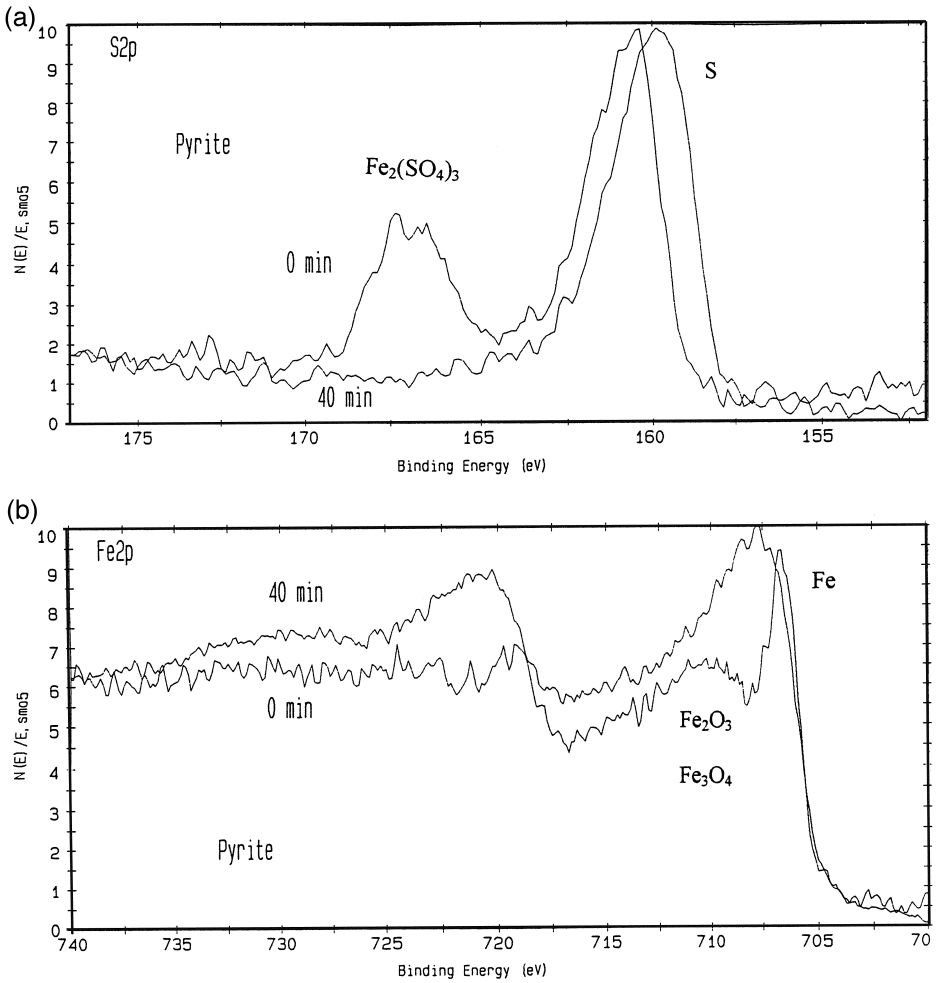

Fig. 9. XPS spectra of finely ground natural pyrite before and after 40-min sputtering (vendor A). (a) S2p binding energy region. (b) Fe2p binding energy region.

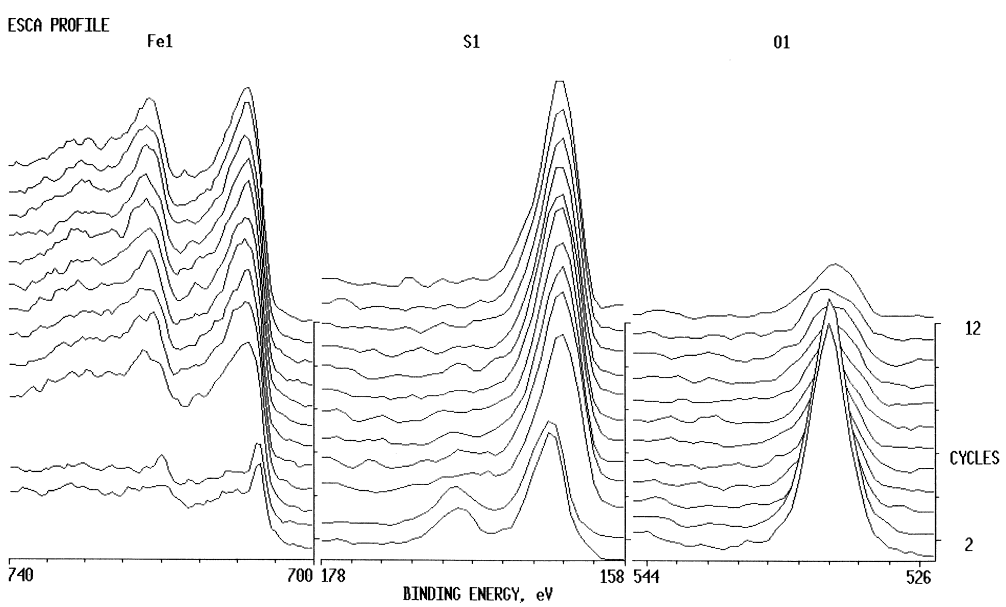

Fig. 10. ESCA profile of < 44 μm natural pyrite (vendor C). The data collected after 40 min of sputtering correspond to cycle no. 12. (a) S2p binding energy region. (b) Fe2p binding energy region. (c)O1s binding energy region.

were used. Particle size was found to affect the thermal stability of pyrite. For a finely powdered (less than 10 μm) vendor-A sample, the major DTG peak of pyrite decomposition is seen at a temperature about 10°C lower than its original value of 648°C (Fig. 4). The additional peaks appear at 346°C, 453°C and 527°C. This phenomenon is associated with the extremely large surface area of the particles, a property that leads to high reactivity. On the other hand, uniform particle distribution increases the thermal stability of pyrite. This can be clearly seen from a comparison of the DTG curves of pristine vendor-E sample (< 44 μm) with those of the 38–44 μm particle size sample (Fig. 5). There is a decrease in the number of low-temperature transitions and overlapping of the two high-temperature (about 500°C) peaks. It is noteworthy that the total weight loss of pyrite from the different sources showed little variation — 23% to 26% up to 700°C independent of the particle size and pretreatment procedure. As determined by our thermogravimetric measurements, the pyrite samples of vendors A, F and G were highly stable up to 500°C. The weight loss of pristine FeS_2 up to this temperature did not exceed 1.3% (Fig. 3 and Table 1).

SEM micrographs of the pristine pyrite (vendor B), presented on Fig. 6, show that the particle size is less than 44 μm.

The particle-separation process of finely ground pyrite, performed by the wet method with the addition of a surface-active agent, resulted in a very low yield particles of 10–15 μm average size. However, a considerable fraction of particles smaller than 10 μm is still present (Fig. 7). The best uniformity — 38 to 44 μm particles — was achieved by repeated pyrite sifting (Fig. 8). The surface area of this sample was less than 0.1 m^2/g.

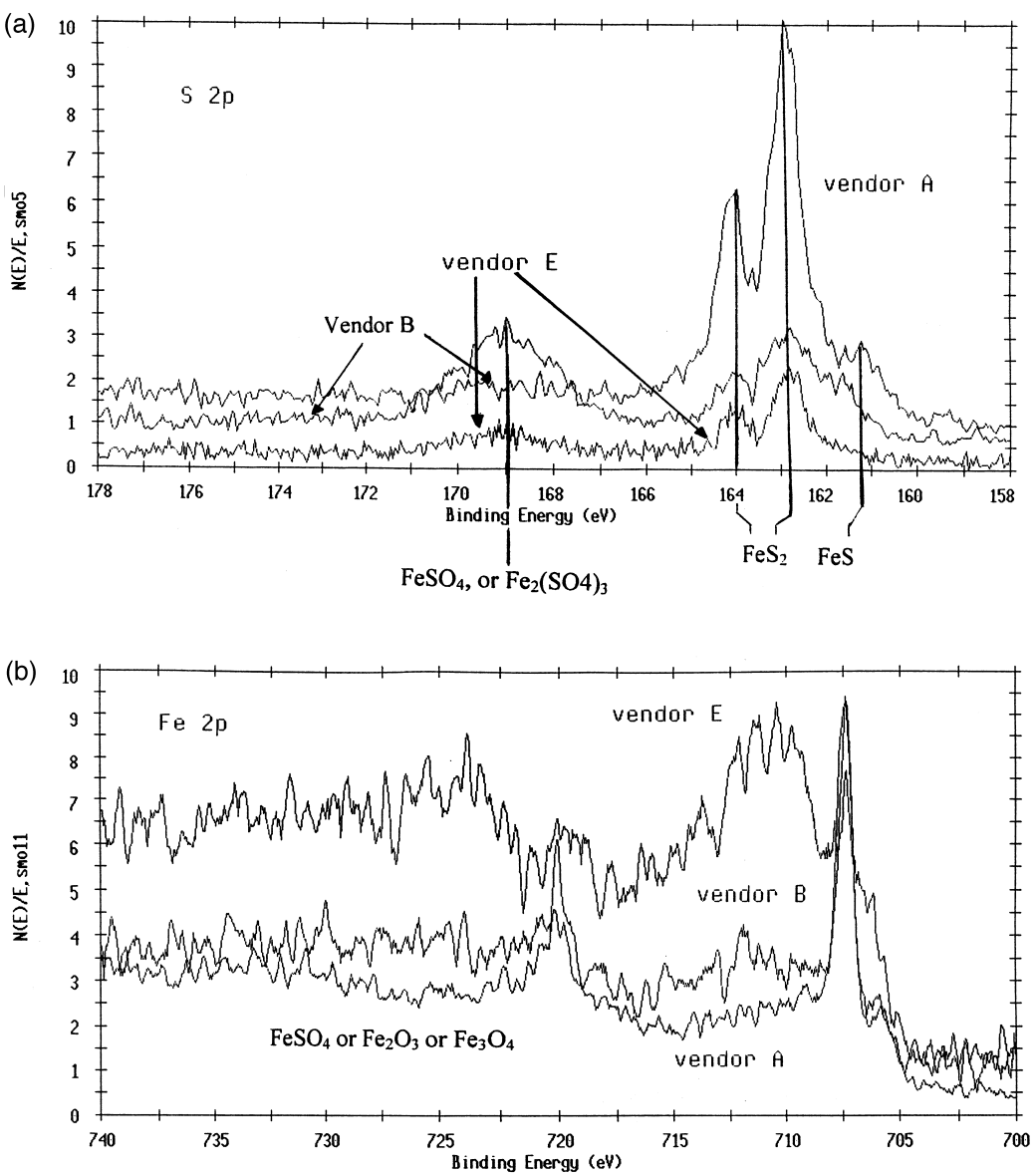

Fig. 11. Nonnormalized XPS spectra of < 44 μm natural pyrite (vendors A, B and E). (a) S2p binding energy region. (b) Fe2p binding energy region.

XPS data of the pyrite powder (< 10 μm, vendor A) before and after sputtering are presented in Fig. 9. Two clear sulfur peaks typical of pyrite (about 162 eV) and iron sulfates $Fe_2(SO_4)_3$ or $FeSO_4$ (about 169 eV) are observed in the S2p-XPS spectrum (Fig. 9a). After 40 min of sputtering (corresponding to removal of 30–50 nm surface layer) the peak at 167 eV, which characterizes the binding energy of sulfur in iron sulfate disappears. The iron-binding energy (Fe2p) region of the XPS spectrum of pyrite is shown in Fig. 9b. There is a doublet peak at 720 and 706 eV characteristic of pyrite [9] and a broad peak at about 710 eV of iron oxides and/or iron sulfates. In addition this peak may also include the FeOOH compound with binding energy 711.3 to 711.8 eV [9].

XPS profiles for iron, sulfur and oxygen of < 44 μm particle-size vendor-B pristine samples are presented in Fig. 10 (a, b and c). The intensity of the S2p line of the pyrite doublet (Fig. 10a) grows with time of sputtering, whereas the peak at 169 eV, which characterizes the binding energy of sulfur in iron sulfate gradually disappears (Fig. 10b). The oxygen signal at 532 eV, typical of iron oxides, deteriorates; however, even after 40 min of sputtering, traces of Fe_2O_3 and/or Fe_3O_4 are still observed. The small shift of the FeS_2 peak on sputtering can be ascribed to partial decomposition of pyrite with the formation of FeS. After 40 min of sputtering, the peaks of the pyrite and surface compounds overlap. The Fe2p XPS peaks of iron oxides and iron sulfates in the iron-binding energy region are in close proximity to each other. The binding-energy peak of the Fe2p line at 712.1 eV correspond to $Fe_2(SO_4)_3$ and those at 710.9 and 710.4 eV to Fe_2O_3 and Fe_3O_4, respectively [9]. Thus, in order to identify the surface compounds more conclusively, the fitting of the Fe2p, S2p and O1s spectra was performed. XPS fitting analysis revealed that pyrite (< 44 μm particle size, vendor B) is covered by a nonhomogeneous layer composed mainly of $FeSO_4$ and iron oxides. The thickness of the surface layer, estimated semiquantitatively, is 30 to 50 nm. In addition it should be mentioned that pyrite surface impurities, such as oxysulfide and iron (II and III) hydrosulfates cannot be excluded. However, it was practically impossible to identify these compounds by XPS measurements. The bulk of the particles is contaminated by Fe_2O_3 or Fe_3O_4. For finely ground pyrite (< 10 μm), the atomic concentration of oxygen increased by about 10% (from 13.3% to 29.6% grinding for 67 h, and 19.7 to 25.3, grinding for 48 h vendor-B sample). A comparison of pyrite from different sources and suppliers showed that pyrite of vendors A and G are the least contaminated (Fig. 11). $FeSO_4$ was found in negligible quantities on the surface. Fe_2O_3 was completely absent even before sputtering. FeS appeared only as a result of partial pyrite decomposition on sputtering. Similar results were found for pyrite of vendor F. The FeS_2 surface of vendor E has the largest content of iron oxides and FeS. It is extremely difficult or even impossible to identify the hydroxide and hydrate derivatives of iron sulfates and oxides by the XPS method. However the XPS data showing, for instance, low contamination of the pyrite surface, are in a good agreement with the high thermal stability of the sample, and

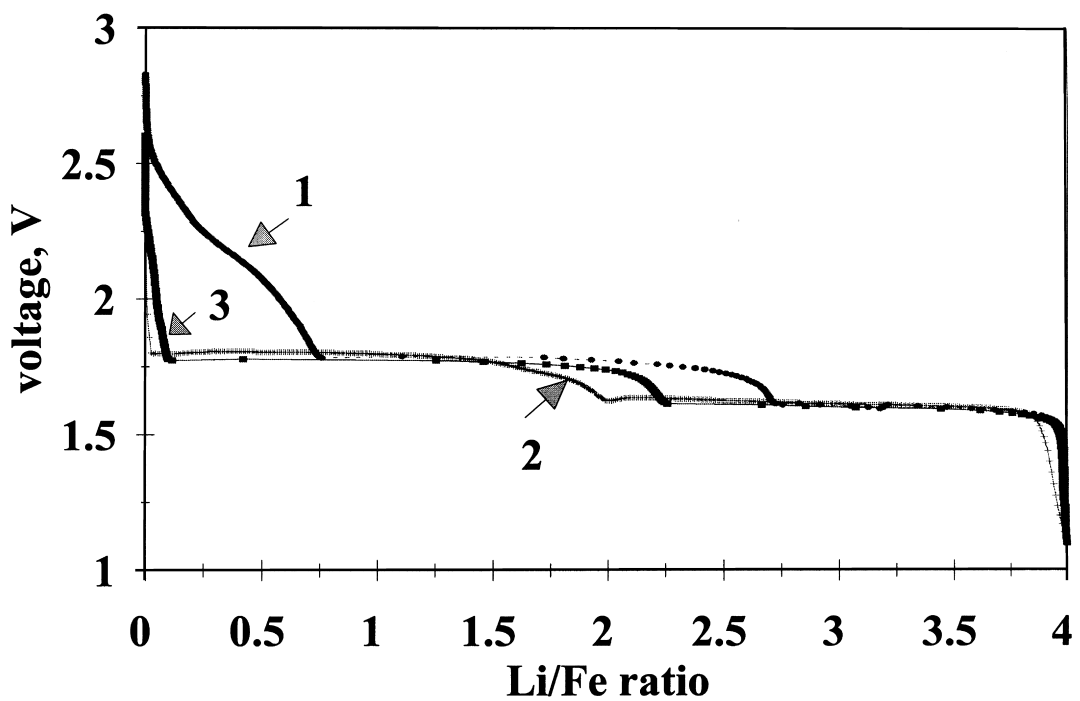

Fig. 12. First discharge of Li/CPE/FeS_2 cell at different preheating time in equilibrium state. Cathode composition: 50% (v/v) FeS_2, 50% (v/v) PE, thickness 10 μm, operating conditions: $T = 135$°C, id = 0.05 mA/cm^2. (1) 2.5 h. (2) 72 h. (3) 100 h.

vice versa: high concentration of iron oxides and sulfates is accompanied by low-temperature weight losses.

The thermal behavior and XPS behavior of synthetic FeS_2, prepared and stored in an inert atmosphere was studied [10]. Surface oxidation products were absent, but a small amount of iron sulfate was found. XPS spectra of synthetic material, exposed to 100% RH (room temperature air) for increasing time periods, show a continuous increase in sulfate concentration. This coincides with increasing weight loss, attributed to the decomposition of iron sulfate at 480°C, just below the main FeS_2 decomposition temperature. The authors found that the high chemical reactivity of the synthetic material, resulting in the formation of surface oxidation products, caused high voltage spikes during the early stages of discharge of the Li alloy/FeS_2 thermal batteries.

Similar results (high initial OCV and discharge voltage) were found for Li/composite polymer or gel electrolyte/pyrite batteries [5,7,11]. OCV values as high as 2.5 to 2.8 V was observed in an as built Li/FeS_2 cell and the first discharge curve had an additional voltage slope at 2.5 to 1.8 V (Fig. 12). The capacity of the high voltage slope at first discharge depends on the source of pyrite and the slope is more pronounced when the cathode is composed of small, less than 10 μm particles. This results from the high surface area of pyrite and its increased sensitivity to the environment and is in agreement with the TGA, BET and XPS data. For more detailed information on the high-voltage slope and to distinguish smaller regions of the coexistence of several phases, dQ/dV vs. V curves were studied. Two or three clear peaks (Fig. 13) are found in a typical dQ/dV plot of the Li/CPE/FeS_2 cell on first

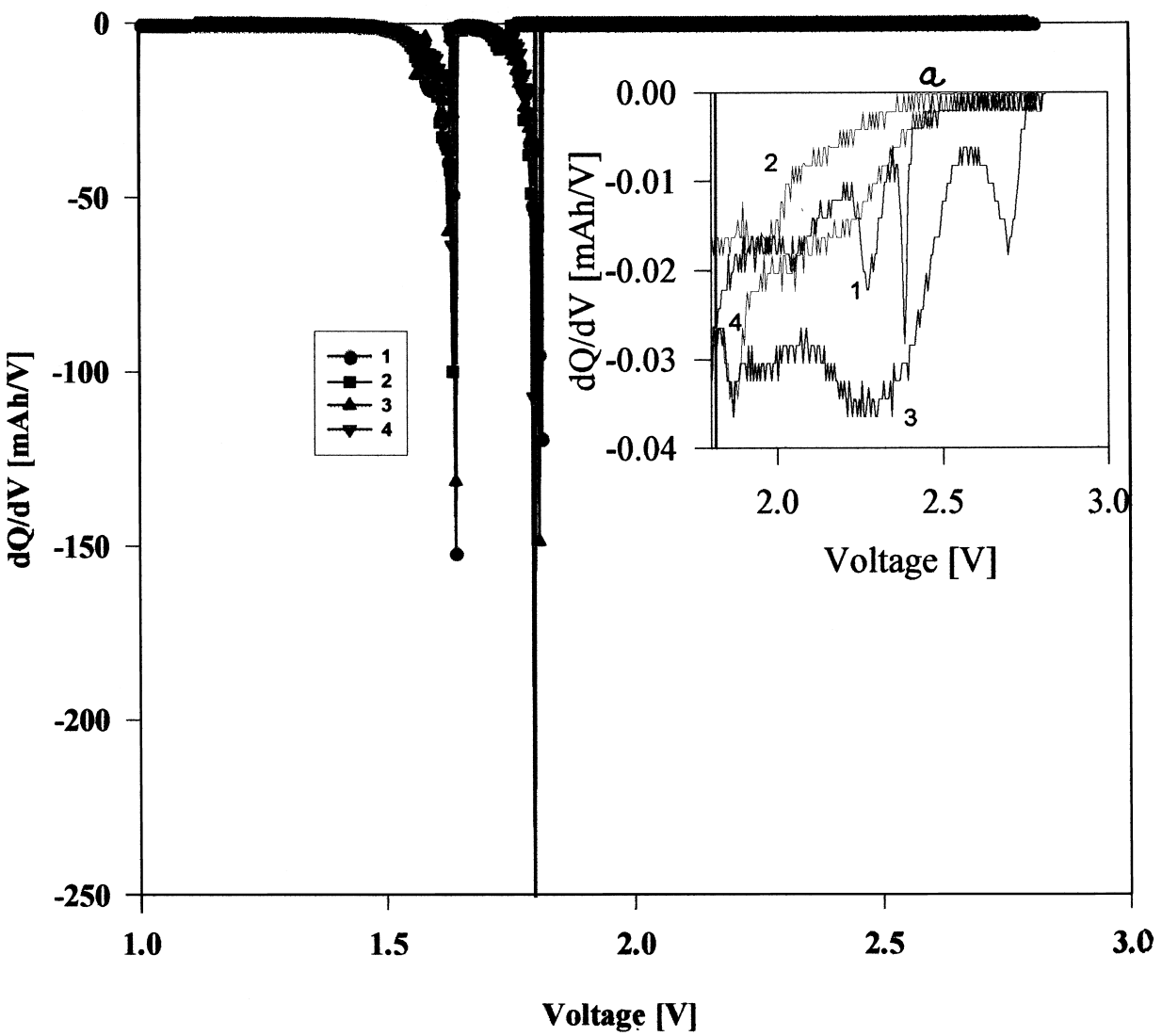

Fig. 13. dQ/dV curves of Li/CPE/FeS_2 cell at cycle 1. Cathode composition: 50% (v/v) FeS_2, 50% (v/v) PE, cathode thickness 45 μm, PE composition: LiI $P(EO)_{20}$ EC_1 12% Al_2O_3. Operation conditions: T = 135°C, id = 0.05 mA/cm^2. (1) Vendor B. (2) Vendor E. (3) Vendor F. (4) Vendor G.

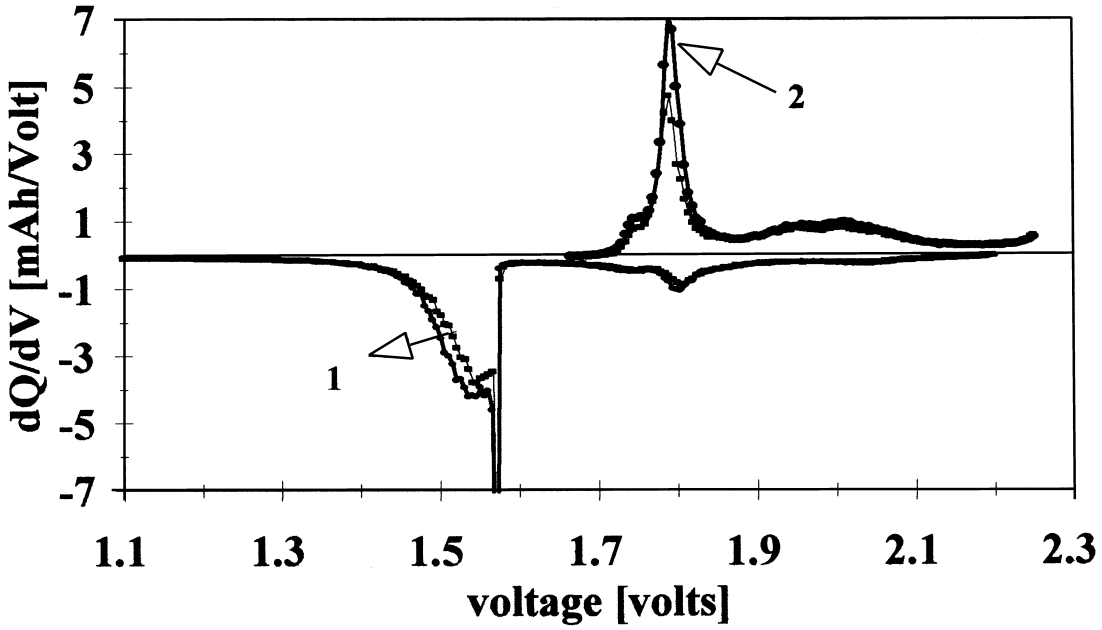

Fig. 14. dQ/dV curves of $Li/CPE/FeS_2$ cell at cycle 2. 10-μm-thick cathode composition: 50% (v/v) FeS_2, 50% (v/v) CPE, CPE composition: LiI $P(EO)_{20}$ EC_1 12% Al_2O_3. (1) Vendor A. (2) Vendor C.

discharge. With the use of EXAFS and NEXAFS techniques it was proved that reduction of the ferrous disulfide proceeds as a multistage process, first to Li_2FeS_2 and finally to metallic iron [12]. Magnification of the 2.5 to 1.8 V region shows several additional peaks at about 2.7 and 2.3 V (Fig. 13a). These may be attributed to the reduction of surface impurities in agreement with their standard reduction potentials vs. Li [8].For instance, the reduction potentials of iron (II and III) hydroxides are 2.1 and 2.5 V vs. Li, respectively, and E^0 of iron (II and III) sulfates are 2.6 and 2.9 V in aqueous solutions. The capacity of the high-voltage peak increases with pyrite contamination, the enlargement of the surface area of cathode material and the alumina content in the cathode. The optimal preheating time of the cells in the equilibrium state to get minimal high-voltage capacity was found to be 48 h. However, it should be mentioned that 45-μm-thick cathode utilization on first discharge is influenced neither by the source of pyrite nor by the uniformity of particle distribution. It varies from 80% to 90% at 50 $\mu A/cm^2$ and 135°C.

All of the subsequent discharge curves of the Li/FeS_2 cell differ from the first indicating a change in the initial mechanism of pyrite reduction. The charge process, which is reversible from the second cycle, ends with the formation of $Li_{2-x}FeS_2$ via Li_2FeS_2 [1,2,4,5,12–17]. Up to seven domains are distinguished on the reversible discharge curve. Three of them correspond to single phases, and the others to multiphase regions. The dQ/dV vs. V plot shows three or four clear peaks on each branch of the charge–discharge curve (Fig. 14). There is another interesting aspect to be emphasized in relation to the pyrite purity. All the characteristic peaks on charge–discharge of 10-μm-thick cathode $Li/CPE/FeS_2$ cell coincide, independent of the pyrite source. The reversible Li/Fe ratio is 2.3–2.5 at 50 $\mu A/cm^2$ and 1.4–1.8 at 300 $\mu A/cm^2$. Similar results were obtained for pyrite cathodes, composed of less than 44 μm and 38–44 μm particles. The degradation rate for 10-μm-thick cathodes, composed of pyrite from vendors A and C was found to be about 1%/cycle after 30 cycles and differs after 70 cycles, 0.8%/cycle for vendor C and 0.6%/cycle for vendor A.

4. Summary

The thermal and electrochemical behavior of pyrite as the cathode material for $Li/CPE/FeS_2$ rechargeable batteries has been investigated. The samples of pyrite from several different sources were characterized by TGA, SEM, XPS and electrochemical analysis. The main result of the present study is the experimental determination that, in spite of the fact that pyrite from different sources is contaminated to different extents, the cells with FeS_2-composite cathodes show similar electrochemical behavior and performance characteristics, such as first-cycle utilization, capacity loss (during the first 30 cycles), Li/Fe ratio and faradaic efficiency. These experimental results are extremely encouraging for battery producers.

Acknowledgements

We would like to thank the Israel Ministry of Energy for financial support.

References

[1] E. Peled, D. Golodnitsky, G. Ardel, J. Lang, Y. Lavi, J. Power Sources 54 (1995) 496.
[2] E. Peled, D. Golodnitsky, E. Strauss, J. Lang, Y. Lavi, Electrochim. Acta 43 (1998) 1593.
[3] R.T. Lowson, Chem. Rev. 82 (5) (1982) 460.
[4] E. Strauss, D. Golodnitsky, G. Ardel, E. Peled, Electrochim. Acta 43 (1998) 1315.
[5] E. Strauss, D. Golodnitsky, E. Peled, Electrochim. Acta (1999) in press.
[6] A. Ennaoui, S. Fiechter, Ch Pettenkofer, N. Alonso-Vante, K. Buker, Ch. Hopfner, H. Tribusch, Sol. Energy Mater. Sol. Cells 29 (1993) 289.
[7] E. Strauss, V. Livshitz, G. Ardel, L. Burstein, D. Golodnitsky, E. Peled, Abstracts of The 64th Meeting of The Israel Chemical Society, Ramat-Gan, Israel, 1999.
[8] Handbook of Chemistry and Physics, CRC Press, 1975–1976.
[9] J. Chastain (Ed.), Handbook of X-Ray Photoelectron Spectroscopy, Perkin-Elmer, USA, 1992.
[10] S. Dallek, B.F. Larrick, B. Beard, P. Pemsler, J.K. Litchfield, R. Lam, in: Proc. 33rd Int. Power Sources Symp., Cherry Hill, NJ, USA 3401987.
[11] G. Ardel, D. Golodnitsky, E. Peled, G.B. Appetecchi, P. Romagnoli, B. Scrosati, Abstracts of The 64th Meeting of The Israel Chemical Society, Ramat-Gan, Israel,1999.
[12] E. Strauss, D. Golodnitsky, E. Peled, S. Kostov, D. Garan, M. denBoer, S. Greenbaum, J. Power Sources (1998) in press.
[13] S.K. Preto, Z. Tomczuk, S. von Winbusch, M.F. Roche, J. Electrochem. Soc. 130 (1983) 264.
[14] R. Fong, J.R. Dahn, C.H.W. Jones, J. Electrochem. Soc. 136 (1989) 11.
[15] R. Brec, E. Prouzet, G. Ouvrard, J. Power Sources 26 (1989) 325.
[16] G.L. Henriksen, Lithium/iron sulfide batteries, in: Handbook of Batteries,1995, pp. 39.1–39.17.